PHYSICAL REVIEW E **94**, 012404 (2016)

# Useful scars: Physics of the capsids of archaeal viruses

L. E. Perotti,* S. Dharmavaram, and W. S. Klug
*Department of Mechanical and Aerospace Engineering, University of California, Los Angeles, California 90095, USA*

J. Marian
*Department of Materials Science and Engineering, University of California, Los Angeles, California 90095, USA*

J. Rudnick
*Department of Physics and Astronomy, University of California, Los Angeles, California 90095, USA*

R. F. Bruinsma
*Department of Physics and Astronomy, University of California, Los Angeles, California 90095, USA*
*and Department of Chemistry and Biochemistry, University of California, Los Angeles, California 90095, USA*
(Received 14 January 2016; revised manuscript received 30 May 2016; published 11 July 2016)

We propose a physical model for the capsids of tailed archaeal viruses as viscoelastic membranes under tension. The fluidity is generated by thermal motion of scarlike structures that are an intrinsic feature of the ground state of large particle arrays covering surfaces with nonzero Gauss curvature. The tension is generated by a combination of the osmotic pressure of the enclosed genome and an extension force generated by filamentous structure formation that drives the formation of the tails. In continuum theory, the capsid has the shape of a surface of constant mean curvature: an unduloid. Particle arrays covering unduloids are shown to exhibit pronounced subdiffusive and diffusive single-particle transport at temperatures that are well below the melting temperature of defect-free particle arrays on a surface with zero Gauss curvature.

DOI: 10.1103/PhysRevE.94.012404

## I. INTRODUCTION

The protein shell—or capsid—that surrounds the genome of a virus has become a proving ground for new methods of microscopy, structure determination, and micromechanics [1]. Viral capsids also provide interesting realizations of the statistical mechanics of interacting particles confined to curved surfaces [2]. Most spherical capsids obey the elegant icosahedral construction principle of Caspar and Klug (CK) [3]. Simulation studies of simple particle models [4] have provided a physical basis for the CK model. Separately, thin-shell elasticity theory has developed into an important tool for understanding the global shape of viral shells [2,5] and the response of viral shells to mechanical deformation [1].

Forty years ago a new domain of life was discovered: the *Archaea* [6]. *Archaea* resemble rodlike bacteria (prokaryotes) in size and shape but their metabolism is closer to that of plant and animal cells (eukaryotes). Other properties, such as the structure of their membranes, are unlike those of either prokaryotes or eukaryotes. Many—though not all—of the *Archaea* survive in extreme environments of high temperatures, salinity, or acidity. They are infected by an equally exotic family of double (ds) or single-stranded (ss) DNA phage viruses: the archaeal viruses [7]. Many archaeal viruses have unusual morphologies (see Fig. 1) that appear to be unrelated to viral capsids that obey the CK construction.

The aim of this article is to develop a physical description for the capsids of a group of archaeal viral shells typified by the spindle-shaped *Acidianus*, a two-tailed archaeal virus (ATV) [11] shown in Fig. 2.

ATV presents a unique characteristic: it undergoes a dramatic shape change outside the host cell. At first, when released from the host, the ATV is lemon- or spindle-shaped and does not have any tails (Fig. 2, top). Subsequently, ATV may grow tails, from opposite ends, that appear to be composed of a cylindrical tube of capsid proteins surrounding a central filamentous structure. Tails may become $\approx 750$ nm long [11]. During tail growth, the ATV loses half of its volume but its area expands only slightly [11], which suggests that the number of capsid proteins is nearly constant. The tail growth process is controlled by the temperature of the surrounding medium [9]: at $T \approx 85\,^{\circ}$C, the tails fully grow in about one hour, at $T \approx 75\,^{\circ}$C complete tail growth occurs in seven to eight days, while at $T \approx 4\,^{\circ}$C no tail growth is detected *in vitro*. Tail growth may increase the probability of contacting a host cell in the surrounding environment [9,11] and it appears that the speed of tail growth is linked to the availability of host cells in the surrounding medium. The tail growth process is the subject of active research motivated by questions about the structure and function of the tails and the source of the energy for the growth of the tails.

We start in Sec. II with a continuum description of the ATV capsid, followed by simulations of models of discrete protein arrays of the ATV capsid in Sec. III. We conclude with a summary and discussion in Sec. IV.

## II. CONTINUUM THEORY OF ATV CAPSIDS

The continuum description of ATV is based on three assumptions.

*Presently at the Department of Radiological Sciences and the Department of Bioengineering, University of California, Los Angeles, California 90095, USA.

 

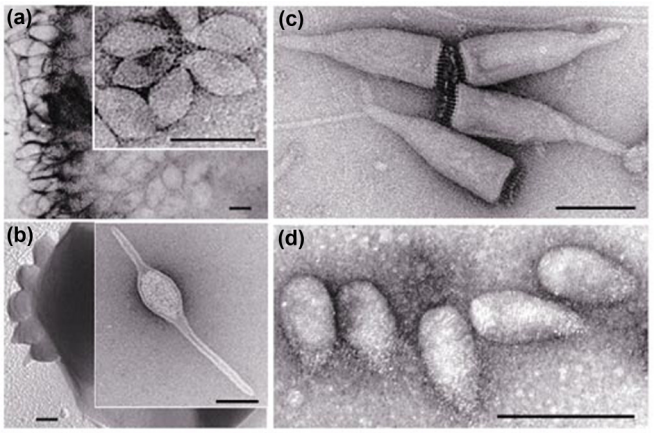


FIG. 1. Electron microscopy images of archaeal viruses. (a) *Sulfolobus* spindle-shaped virus. (b) *Acidianus* two-tailed virus (ATV). (c) *Acidianus* bottle-shaped virus. (d) *Sulfolobus neozealandicus* droplet-shaped virus. Scale bars equal to 100 nm. Reprinted by permission from Macmillan Publishers [8]. Originally adapted from Refs. [9] and [10].

(i) The protein capsid of the ATV virus is a closed, isotropic, fluid or viscoelastic sheet of fixed area $A$. This is motivated by the fact that the massive conformational changes observed for the ATV capsid are inconsistent with positionally ordered capsid proteins.

(ii) The conformational change of the ATV capsid with temperature is assumed to be driven by the growth of a central, cylindrical filamentous structure. We will define $L$ to be the length of this filament and $a$ its radius. The assembly free-energy gain per unit length of filament, the extension force, will be denoted by $\tau$. This extension force refers to bare filament sections not adhering to capsid material. The adhesion free-energy gain per unit length due to attractive interactions between the capsid proteins and the filament will be denoted by $w$. If capsid proteins in contact with filament material undergo any conformational changes then this is to be included in $w$.

(iii) The enclosed genome is a uniform, isotropic fluid or viscoelastic medium in a state of mechanical equilibrium.

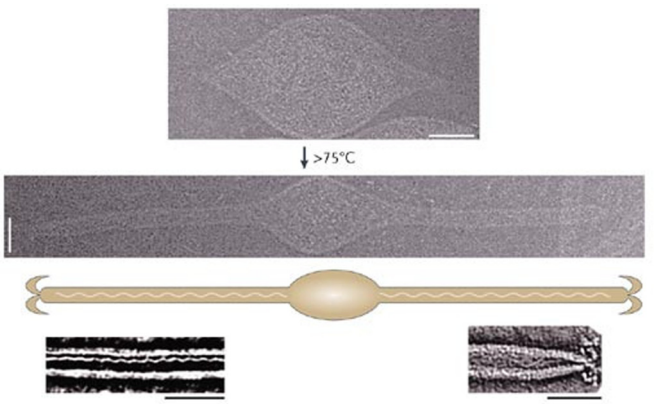


FIG. 2. Cryoelectron micrographs of the conformational change of ATV and its reconstruction. Scale bars represent 50 nm. Reprinted by permission from Macmillan Publishers [8]. Originally adapted from Ref. [11].

This means that the free-energy per unit volume $f$ of the genome can depend only on the density of the enclosed double-stranded (ds) DNA material. The ratio $V_m/V$ will serve as a dimensionless measure of the density of the enclosed DNA material. Here, $V$ is the capsid volume and $V_m$ is the minimum volume of the 62 kbp double-stranded (ds) ATV DNA genome. $V_m$ can be estimated to be about $3 \times 10^5$ nm$^3$, assuming standard ds B-DNA parameters. The volume $V$ of an ATV capsid before tail growth is about twice larger than the volume of the capsid with fully extended tail groups, so the genome density roughly doubles during tail growth.

The large change in volume means that the capsid must be water permeable. As a result, the genome must exert a uniform osmotic pressure $\Pi$ on the capsid (Pascal's law). The osmotic pressure is related to the free-energy density $f(V_m/V)$ by $\Pi = -f + (V_m/V)f'$. The equation of state $\Pi(V_m/V)$ of aligned DNA has been measured in osmotic compression experiments of DNA bundles [12,13]. In the absence of condensing agents, the osmotic pressure is about $10^4$ Pa at half the maximum B-DNA packing density, and this will be our estimate of the ATV osmotic pressure before tail growth. The osmotic pressure inside ATV capsids after tail growth is more difficult to estimate. Osmotic pressures inside the $\lambda$ phage virus, which has a genome length comparable to ATV, have been measured to be in the range of $10^6$ Pa [14]. These very large osmotic pressures are believed to be an important driving agent for the injection of the viral genome into host cells [14].

In this description, the total continuum free energy has the general form

$$G = fV + \gamma A - \tau L - 2wX. \tag{2.1}$$

Here, $\gamma$ is the surface tension of the capsid generated by the osmotic pressure. The assumption of fluidity of the capsid means that $\gamma$ is uniform along the capsid surface under conditions of mechanical equilibrium. Next, $2X$ is the length of two symmetric, capsid-covered tail sections extending from the central body of the capsid of volume $V$.

Based on Fig. 2, we look for minima of this free energy in the shape of a body of revolution matched to the capsid-covered tail sections at matching points that are a distance $\pm(L - 2X)/2$ from the center (Fig. 3). Minimizing the free energy first with respect to the overall filament length $L$ while keeping the

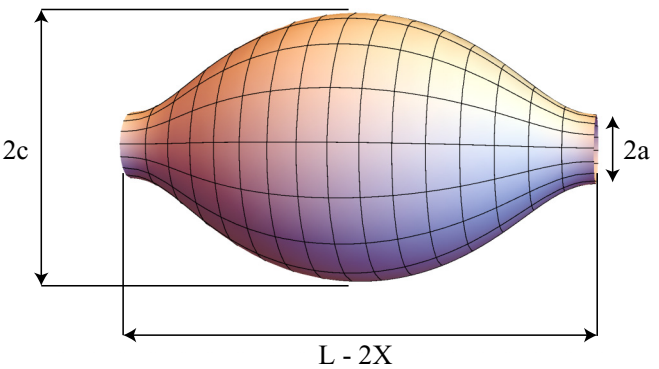


FIG. 3. Capsid with zero contact angle in the shape of an unduloid. The smallest diameter is $2a$, the largest diameter is $2c$.

central body fixed—so for a fixed value of $(L - 2X)/2$—leads to the condition

$$\tau + w = 2\pi a\gamma. \tag{2.2}$$

Next, minimizing $G$ with respect to $X$ at fixed $L$ leads to

$$w/(2\pi a) = \gamma(1 - \cos\theta), \tag{2.3}$$

with $\theta$ the contact angle between the central body of the capsid and the filament at the two matching points. This is Young's law of the general theory of wetting [15]. Finally, minimization of $G$ with respect to the shape of the capsid leads to the Laplace law [15]

$$\Pi = 2\gamma H. \tag{2.4}$$

Here, $H$ is the local mean curvature of the capsid surface. Since, by assumption, the osmotic pressure of the interior of the virus is uniform and since $\gamma$ is uniform as well, the capsid surface must be a surface of constant mean curvature. For ATV osmotic pressures in the range of $10^4$ Pa and mean curvatures in the range of $1/(100\text{ nm})$, the surface tension would be in the range of $5 \times 10^{-4}$ N/m.

There are only a few surfaces of constant mean curvature with axial rotational symmetry and, of these, only the unduloid surfaces [16] resemble ATV capsids.[1] Unduloids are surfaces of revolution obtained by rotating an elliptical catenary [17]. Figure 2 (bottom micrograph) suggests that for ATV capsids with fully developed tails the contact angle is small or zero.[2] In the following we will assume for simplicity that $\theta = 0$ so $w = 0$. According to Eq. (2.2), this means that $\gamma = \tau/(2\pi a)$. For the estimated value of the surface tension, the extension force $\tau$ of the ATV central filament would be in the range of 50 pN.

The unduloid shape with zero contact angle is shown in Fig. 3 and it is fully determined by the smallest and largest diameters $2a$ and $2c$. The constant mean curvature $H$ of the body of the capsid equals $1/(a + c)$. The mean curvature of the capsid covering the tail groups equals $1/a$, so there is a mathematical singularity at the matching points.

If we define the parameter $k$ as $k^2 = 1 - (a/c)^2$ then the dimensionless volume $V/c^3$, area $A/c^2$, and length $(L - 2X)/c$ of the unduloid can be expressed in terms of $c$, using results from Ref. [16]:

$$V/c^3 = \frac{2\pi}{3}\{[2 + 3(a/c) + 2(a/c)^2]E(k) - (a/c)^2 K(k)\}; \tag{2.5}$$

$$(A - 4\pi aX)/c^2 = 4\pi(1 + a/c)E(k); \tag{2.6}$$

$$(L - 2X)/c = 2E(k) + 2(a/c)K(k), \tag{2.7}$$

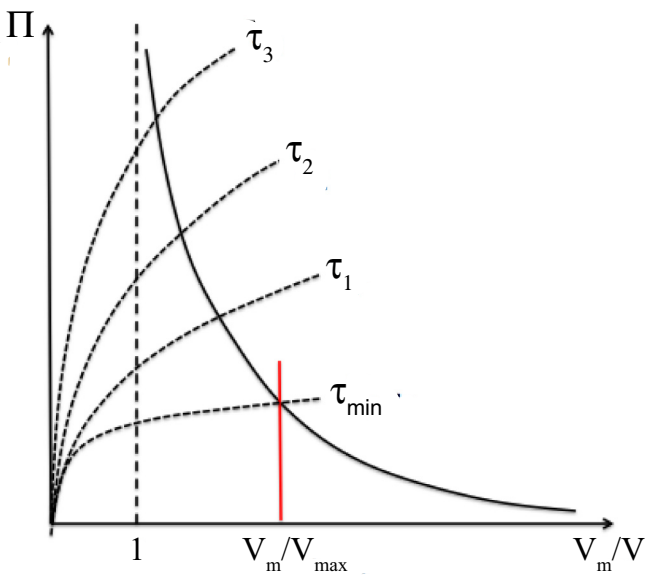


FIG. 4. Graphical construction for the capsid volume. Vertical axis: osmotic pressure Π. Horizontal axis: dimensionless density $V_m/V$ with $V_m$ the minimum volume corresponding to densely packed double-stranded (ds) DNA. Solid black line: Schematic equation of state of ds DNA under physiological conditions in the absence of condensing agents. The osmotic pressure diverges at $V_m/V = 1$. Dashed curves: $\tau/[\pi a(3V/4\pi)^{1/3}]$ for different values of the extension force $\tau$. At the minimum value $\tau_{\min}$, the length $L$ of the central filament equals the diameter $2c$ of the unduloid

where $K(k)$ and $E(k)$ are complete elliptical integrals of the first and second kind. Moreover, the Laplace law reduces to

$$\Pi(V_m/V) = \tau/[\pi a(a + c)]. \tag{2.8}$$

These equations are to be solved by first inverting Eq. (2.5) to express $c(V)$ in terms of the volume $V$. Next, the intersection of a plot of the equation of state $\Pi(V_m/V)$ as a function of $V$ with $\tau/[\pi a(a + c(V)]$ determines the volume $V$ for different values of $\tau$ and hence $c$. The values of $X$ and $L$ as a function of $\tau$ then follow from Eq. (2.6), respectively, (2.7). An example is shown in Fig. 4 for a schematic form of $\Pi(V_m/V)$ and for the case that the ratio $c/a$ between the largest and smallest unduloid diameter is large compared to one. In that case Eq. (2.5) reduces to $c(V) \simeq (3V/4\pi)^{1/3}$.

For increasing extension forces $\tau$, the enclosed volume shrinks and approaches the close packing limit $V_{\min}$. The capsid becomes increasingly elongated with increasing $\tau$, consistent with Fig. 2. With decreasing $\tau$, when $c$ increases, $X$ shrinks as $L/2 - c(V)$ according to Eq. (2.6) and vanishes at a critical extension force $\tau_{\min}$, where the area of the unduloid equals the maximum available area $A$ and $L = 2c(V)$.

For $\tau$ less than $\tau_{\min}$, the capsid surface no longer has the shape of an unduloid. It is in contact only with the very tip of the filament. This regime of small $\tau$ is most easily treated by starting from the case that there is no central filament. In the absence of a central filament, the capsid is spherical with a radius $R_0$ subject to the minimum osmotic pressure $\Pi_0(V_m/V_0) = 2\gamma_0/R_0$. The radius $R_0$ is determined by the fixed area constraint $A = 4\pi R_0^2$, which fixes the volume as $V = (4/3)\pi R_0^3$. The minimization of $G$ reduces to the problem

[1]There is an interesting resemblance between the shape of an ATV capsid at various stages of tail growth with that of droplets wetting a cylindrical fiber, which indeed are described by unduloids.

[2]It is possible that the contact angle is actually nonzero but that the capsid profile is smoothed out because of the effects of a large Helfrich bending energy.

of determining the shape of a circular sheet of radius $R$ with a tension $\gamma_0$ subjected to a point force $\tau$ exerted in the normal direction. This is a standard exercise [15], leading to a protrusion profile $\zeta(r) = \zeta \ln(R/r)/\ln(R/a)$ where $\zeta$ is the maximum height of the protrusion. This profile should correspond to the two protrusions of Fig. 2 (top micrograph). The corresponding energy is

$$G(\zeta) \simeq [4\pi\gamma_0/\ln(R_0/a)]\zeta^2 - 2\tau\zeta. \tag{2.9}$$

The capsid tension thus generates a harmonic restoring force for $\zeta$. Minimizing with respect to $\zeta$ gives a linear force-displacement curve:

$$\zeta(\tau) \simeq \tau/[4\pi\gamma_0/\ln(R_0/a)]. \tag{2.10}$$

As an example, for the protrusion to have a size in the range of 10 nm with a tension $\gamma_0$ in the range of $5 \times 10^{-4}$ N/m, the polymerization force $\tau$ must be in the range of 50 pN, consistent with the earlier estimate. "Passive" polymerization forces near thermal equilibrium, as measured for microtubules and actin filaments, are in the range of 10 pN or less [18], which suggests that the polymerization force for the ATV central filament is an active process involving consumption of ATP.

The full force-extension curve is obtained by matching the linear and nonlinear regimes at $\tau = \tau_{\min}$ as shown in Fig. 5.

This continuum theory is, at least qualitatively, consistent with the currently available observations for the case of ATV with fully extended tail groups. The increase in osmotic pressure produced by the tail growth suggests that one of the roles of the ATV shape change is to prime the capsid for release of the genome through one of the tails after the virus has attached itself to a host cell.

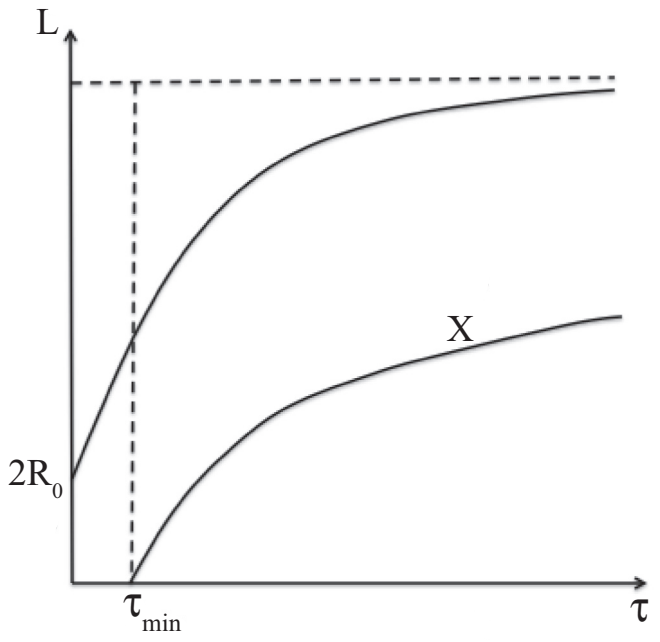


FIG. 5. Force-extension curve of the central filament as a plot of filament length $L$ versus extension force $\tau$. For $\tau$ less than $\tau_{\min}$, when the length $X$ of the tails is zero, the filament only indents the capsid and the force-extension curve is approximately linear. For larger values of the extension force, the capsid develops tails. The area of the capsid limits the maximum value of the filament length.

If assumption (i) of continuum theory, capsid fluidity, indeed is valid then this sets ATV capsids apart from CK viral capsids in a fundamental way. The CK construction for viral capsids is based on the assumption that the capsid proteins form an ordered array. So under which conditions could viral capsids be in a fluid state? It is certainly possible to generate capsid fluidity by reducing the energy scale for attractive interactions between capsid proteins towards the thermal energy $k_BT$. However, capsid fluidity has to be consistent with the requirement that the ATV capsid is strong enough to absorb the tension generated by the osmotic pressure of the enclosed genome, which we estimated to be of the order of $5 \times 10^{-4}$ N/m or larger. In the next sections we will use numerical modeling to explore under what conditions a viral capsid can have a sufficient amount of capsid protein transport from the main body of the capsid to the tails on relevant time scales while retaining a sufficient level of lateral stiffness to absorb the tension.

## III. SIMULATIONS OF ATV CAPSID PROTEIN ARRAYS

Simulations were performed on particle arrays placed on scaffolds with various shapes. The particles interacted with each other via radial pair potentials with a minimum at a spacing $r_m$ of 6 nm with variable binding energy $\epsilon$. These particles do *not* represent individual ATV capsid proteins. Instead, they represent—in a coarse-grained representation—oligomers composed of five, six, or seven proteins, known as capsomers. The minimum spacing $r_m$ between the particles is about twice the size of a capsid protein. It should be noted though that currently it is not known if ATV subunits indeed preassemble into capsomers. However, in many known cases the proteins of viral capsids preassemble into roughly circular pentamer and hexamer oligomers. A radial pair potential, with short-range repulsion representing the relative incompressibility of capsomers and the longer-range attraction representing hydrophobic attraction between the rims of the capsomers, is a crude but reasonable coarse-grained potential for the interaction between protein capsomers. Particle arrays of this type placed on spherical surfaces have earlier been shown to reproduce the CK construction [19] of small spherical viral capsids so they are the natural starting point for numerical models of ATV.

About $10^3$ of these particles, the estimated number of capsomers of an ATV capsid, were placed on unduloid scaffolds based on the CK construction principle (Sec. III A). We used Monte Carlo (MC) annealing to test whether the CK constructed states were in fact ground states. Next, we carried out kinetic Monte Carlo (KMC) simulations and evaluated the mean-square displacements (MSDs) of the particles as a function of time. From the MSDs we obtained particle transport rates for different values of $\epsilon$. We also carried out KMC simulations on spheres and cylinders in order to compare with particle kinetics on spherical capsids in the absence of the tails, and particle kinetics on the cylindrical tails. Finally, we placed the particle array under tension in order to verify the Laplace's law of continuum theory and the ability of capsids in the fluid state to absorb tension.

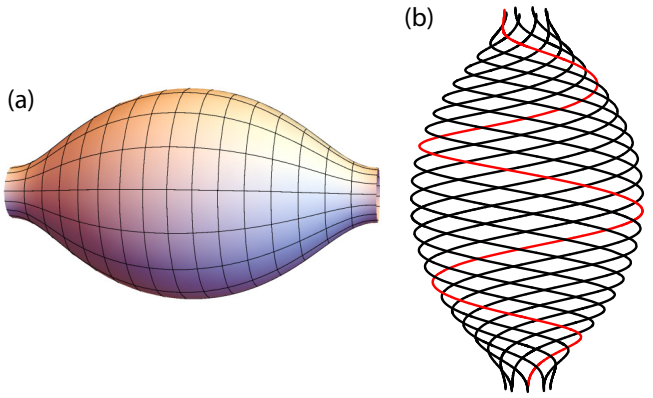


FIG. 6. Spiral construction: (a) Initial unduloid. (b) Eight equidistant spirals covering the unduloid surface and constructed according to the method of Appendix B (one spiral is colored in red to highlight spacing).

### A. Caspar-Klug construction for unduloid capsids

The CK construction for the capsids of cylindrical viruses [3] places capsid proteins along an array of interlocking, equidistant spirals of fixed pitch (Archimedean spirals) and radius where every protein has the same local symmetry as every other protein. In order to construct similar particle arrays on an unduloid, we covered the unduloid with Archimedean spirals separated by a constant spacing [see Fig. 6(b)]. In Appendix B, we construct a general differential equation for curves covering surfaces of revolution. In Fig. 6(b) we show an unduloid covered by eight of these spirals. The minimum pitch is reached at the maximum diameter of the unduloid, after which the pitch increases again in a symmetric fashion.

Next, we placed particles along the spirals that interacted with each other via a Lennard-Jones (LJ) pair potential given by

$$V(r) = \epsilon[(r_m/r)^{12} - 2(r_m/r)^6]. \tag{3.1}$$

Here, $r$ is the spacing between two particles, $\epsilon$ the binding energy, and $r_m$ the interparticle spacing at the minimum of $V(r)$. The spacing between the spirals was equal to $\approx r_m$. Particles were placed sequentially along the spirals starting from the two endpoints, as shown in Fig. 7.

As particles were added, the particle array was periodically allowed to relax by letting the particles make random moves, followed by a zero-temperature Monte Carlo relaxation step. An unduloid can be almost completely covered by this method, apart from a few small gaps around the equator that were filled by hand. If this same procedure is applied to five equidistant spirals covering a sphere then the $T = 7$ and $T = 13$ CK construction is recovered (e.g., see Fig. 23 in Appendix B).

In order to visualize the capsomers represented by the particles, we performed a Voronoi tessellation, as shown in Fig. 8. Voronoi cells with five edges, colored blue, represent pentamers, cells with six edges, colored gray, represent hexamers, while cells with seven edges, colored red, represent heptamers. For comparison, an icosahedral particle array covering a sphere is composed of hexamers plus twelve pentamers distributed over the vertices of an icosahedron [e.g., see Fig. 12(a)].

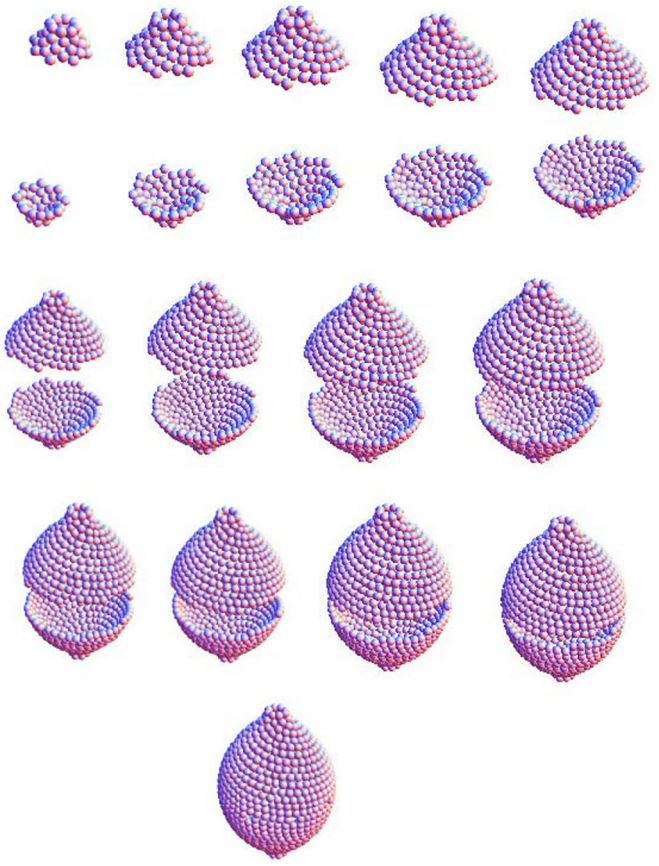

FIG. 7. Sequential placement of particles on the eight helices covering the unduloid of Fig. 6. The arrays is constructed first on two half unduloids, which are then merged. Any holes left after merging are filled with particles

Isolated heptamers and pentamers can be viewed as sevenfold, respectively, fivefold *disclination defects* of a hexagonal array of capsomers, while heptamer-pentamer pairs can be viewed as *dislocation defects* [20]. In Fig. 8(a), two rings of isolated dislocations can be seen to surround the unduloid midway between the equator and the necks of the unduloid, while a ring of dislocation pairs surrounds the equator. Next, in Fig. 8(b), a view of the unduloid along its axis shows eight strings of dislocations emerging in a spiral pattern from the two endpoints as well as an accumulation of heptamers near the ends. Such dislocation strings can be viewed as *grain boundaries* of a hexagonal lattice.[3]

### B. Monte Carlo annealing

In order to determine whether the CK construction corresponds to the ground-state configuration, we carried out annealing Monte Carlo simulations of unduloids covered by particle arrays placed according to the spiral construction

[3]The appearance of the grain boundaries can be understood by cutting eight identical adjoining triangular wedges from the ends of a cylindrical tube. Gluing together the edges of these adjoining triangles produces eight grain boundaries. The spiral arrays at the ends of the unduloid is a twisted version of this construction.

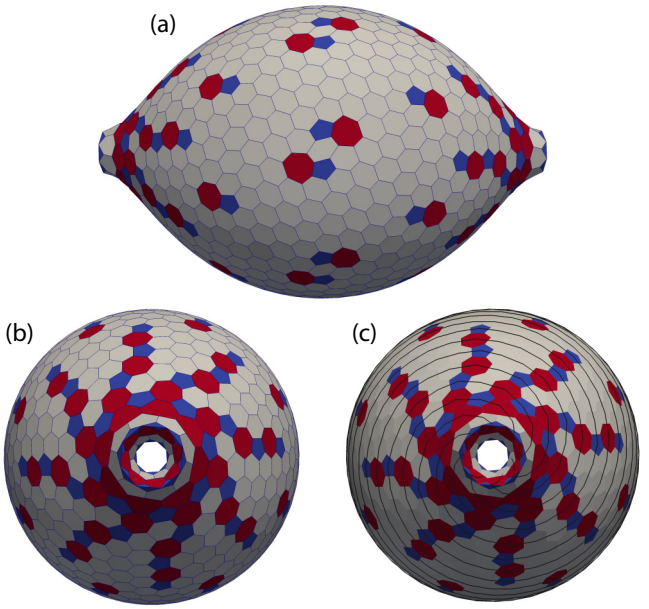


FIG. 8. Voronoi construction corresponding to the initial particle configuration covering the unduloid. Cells with five edges are colored blue (pentamers), cells with six edges gray (hexamers), and cells with seven edges red (heptamers). (a) Side view showing isolated dislocations. (b) Front view showing eight spiral dislocations strings. (c) Front view overlaid with construction spirals.

method and interacting via LJ potentials. The particle positions were constrained to a discrete mesh with a mesh size $a$ that was small compared to the lattice constant $r_m$ of the particle array ($a = r_m/16$). We imposed fixed boundary conditions at the two necks of the unduloid by fixing in place eight particles forming rings at the ends of the unduloid. The system was initially heated to a temperature well above the binding energy $\epsilon$ of the LJ potential after which the temperature was slowly reduced back to nearly zero ($T \sim 10^{-3}\epsilon$). Further details of the simulated annealing procedure are summarized in Appendix C. The annealing procedure was first performed for the case of about 1000 particles placed on a cylinder in the hexagonal ground-state configuration. The heating pulse produced large amounts of heptamers and pentamers [Fig. 9(b)]. After annealing, the system returned to the defect-free ground state [Fig. 9(c)].

We then repeated the annealing procedure for an unduloid covered by 920 particles. Figure 10 shows the initial state (the spiral construction), a snapshot of an intermediate state with large disorder shortly after the heating pulse, and a snapshot of the final state.

As a consequence of the annealing, the spiral grain-boundary defects that initially were attached to the endpoints in the CK construction broke free from the ends of the unduloids and ended up as free-floating dislocation strings. The detached strings were either charge neutral, i.e., with equal numbers of pentamers and heptamers, or the number of pentamers exceeded the number of heptamers by one.

These observations are consistent with the fact that particle arrays placed on surfaces with positive Gauss curvature lower their elastic energy by the introduction of fivefold

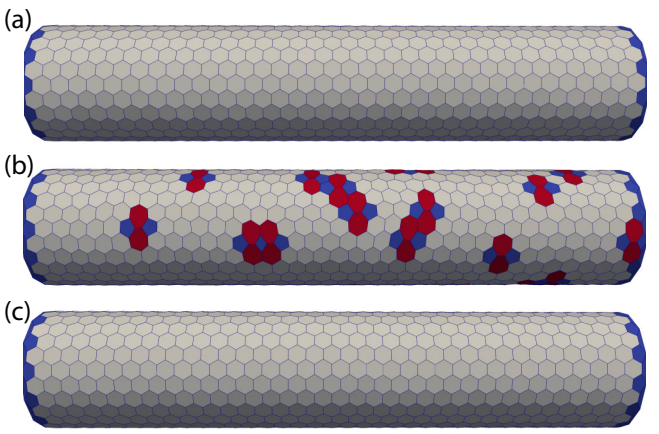


FIG. 9. Annealing of a cylinder. (a) Initial state; (b) intermediate state after the heating pulse; and (c) final state.

disclinations [20,21], while sevenfold disclinations lower their elastic energy in saddlelike sections of the surface with negative Gauss curvature [22] (see also Fig. 16). Finally, dislocations minimize their elastic energy in surface sections with zero Gauss curvature. Mobile disclinations and dislocations placed on an unduloid will, at finite temperatures, perform some form of Brownian motion in this curvature-determined energy landscape that is also influenced by interactions between the defects.

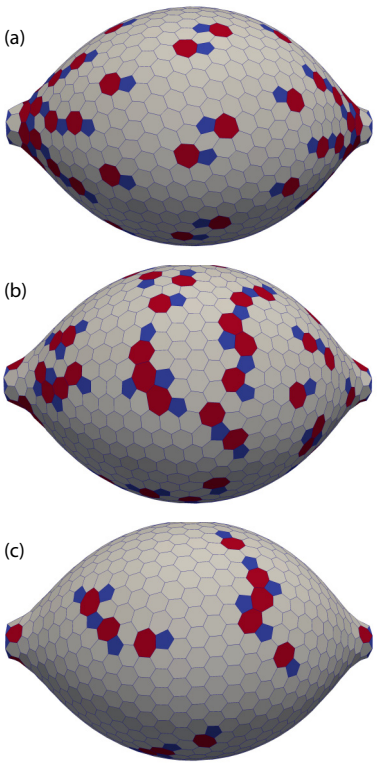


FIG. 10. Monte Carlo annealing. (a) Initial state with spiral order. (b) Intermediate state after heating pulse (images corresponds to 1000 Monte Carlo steps, see also Fig. 11). (c) Final state.

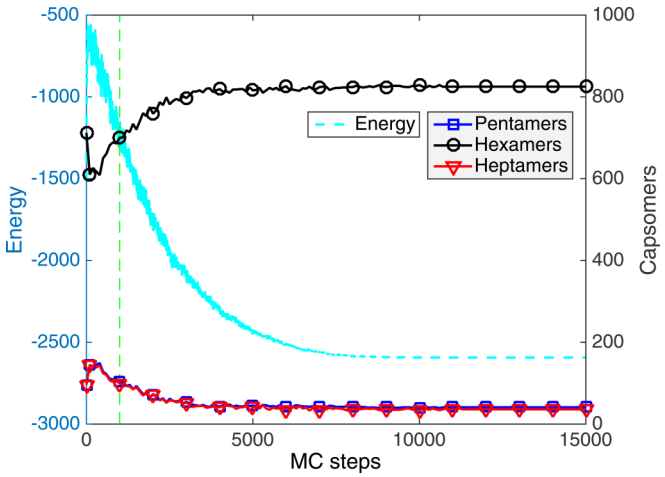


FIG. 11. Evolution of the energy (left vertical axis) and capsomer numbers (right vertical axis) versus Monte Carlo steps during the annealing of an unduloid. The vertical dashed line corresponds to the intermediate state shown in Fig. 10(b).

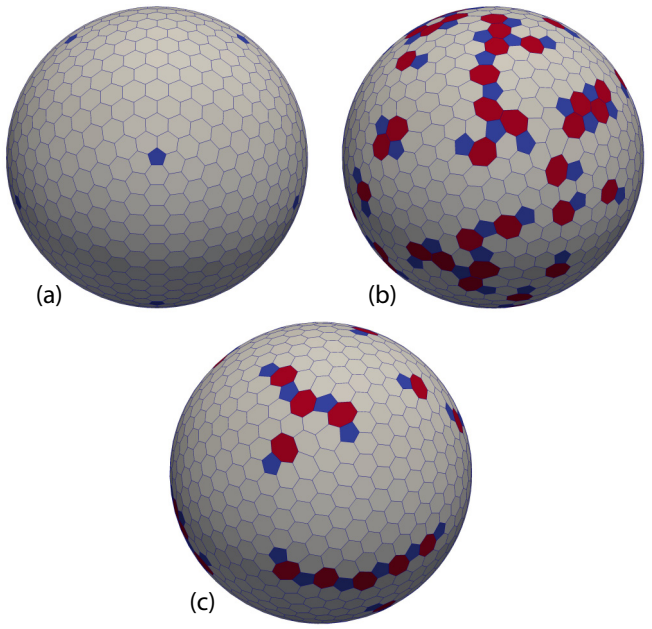


FIG. 12. Annealing of a particle array covering a sphere. (a) Initial, (b) intermediate (image corresponds to about 1/8 of the annealing simulation time), and (c) final configurations.

The total interaction energy and the number of pentamers, hexamers, and heptamers is shown in Fig. 11 as a function of the number of MC steps. Following the heating step, the energy increased very rapidly from an initial value of about $-1500\epsilon$ for the spiral structure to a highly defected state with an energy of about $-500\epsilon$. During cooling, the energy decreased to approximatively $-2600\epsilon$, which is well below the energy of the CK spiral construction. In the final state, the number of hexamers has increased while the number of pentamers and heptamers has decreased.

We can conclude that for particle arrays interacting with a radial pair potential of the LJ form, the CK spiral construction is not the lowest-energy state for an unduloid.

We repeated the annealing procedure for the case of a spherical shell covered by 1002 particles, starting from a $T = 100$ CK icosahedral state (Fig. 12). After Monte Carlo annealing, this array also did not return to the CK state (Fig. 12 c). The final state was again defected and had a lower energy ($\simeq -3100\epsilon$) than the CK state ($\simeq -2400\epsilon$). The final state of the sphere was again characterized by free-floating scars.

Particle arrays covering spherical surfaces are in fact known to undergo a transition as a function of sphere radius from a state with 12 fivefold disclinations to a state with a distribution of grain-boundary type scars [23]. These scars relax the elastic stress that accumulates around the fivefold disclinations when the size of the sphere increases. As a check, we repeated the annealing procedure for a small CK shell (a $T = 7$ shell, see Appendix E) and found that this shell indeed had no defects in the final configuration, apart from the 12 pentamers.

We conclude that the defect strings distributed over the central section of the unduloid have the same physical origin as the scars that are present in the ground state of particle arrays covering large spherical surfaces.

### C. Mean-square displacement and viscoelasticity

In order to examine the transport properties of unduloid-shape capsids, we next carried out kinetic Monte Carlo (KMC) simulations with particles performing a Brownian random walk on the underlying fine discrete mesh. The bare diffusion coefficient $D_0 \propto a^2\nu_0$ of single particles on the mesh, with $1/\nu_0$ the KMC time step and $a$ the mesh size, was kept fixed, which means that the temperature was fixed (further details are summarized in Appendix D). Initial states were produced by the annealing method presented in Sec. III B, except for the sphere for which we adopted the CK construction as the initial state. We computed mean-square displacements (MSDs) as a function of time for different values of the dimensionless inverse binding energy $k_BT/\epsilon$ of the LJ interaction potential. Specifically, we increased $k_BT/\epsilon$ by increments of 0.75 between adjacent MSD plots (as marked on some of the curves in Figs. 13 and 14).

Figure 13 shows MSD versus time plots for the case of cylindrical surfaces.

For comparison, we show also the MSD versus time plot for a single-particle (black line), which is linear on a log-log scale with slope one, as expected for simple diffusion. The MSD plots for the interacting particles can be divided into two groups. For $k_BT/\epsilon$ less than or equal to 3.25, the late-time MSD is, within error bar, independent of time. For $k_BT/\epsilon$ larger than or equal to 4.00, the slope of the late-time MSD-time plots is close to one, consistent with single-particle self-diffusion. This suggests that a melting transition takes place at a value of $k_BT/\epsilon$ between 3.25 and 4.0. The self-diffusion coefficient is in general not an ideal dynamical characteristic for melting transitions because self-diffusion coefficients are not zero below a melting transition [24]. However, simulation studies of arrays of particles interacting via LJ pair potentials, either with periodic boundary conditions [25] or as particle clusters [26], report that around the melting transition the self-diffusion coefficient does increase by more than an order of magnitude over a small temperature interval. This is consistent

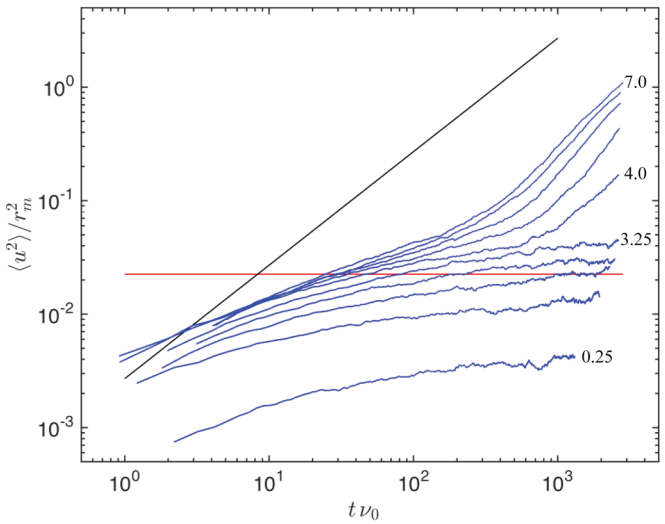


FIG. 13. Mean-square displacement (MSD) $\langle u^2\rangle/r_m^2$ on a cylinder versus time on a log-log scale. Time is expressed in units of the inverse step frequency $\nu_0$ and distance in units of $r_m$, the equilibrium spacing of the LJ pair potential. The dimensionless inverse potential depth $k_BT/\epsilon$ is increased in multiples of 0.75 as indicated for some of the curves. The horizontal line is the MSD of a hexagonal lattice at the melting point. The black solid line is the MSD of an isolated particle.

with the rapid onset of self-diffusion seen in Fig. 13, so it is indeed reasonable to assume that a melting transition did take place for $k_BT/\epsilon$ between 3.25 and 4.0. Interestingly, numerical simulations of two-dimensional LJ hexagonal arrays report

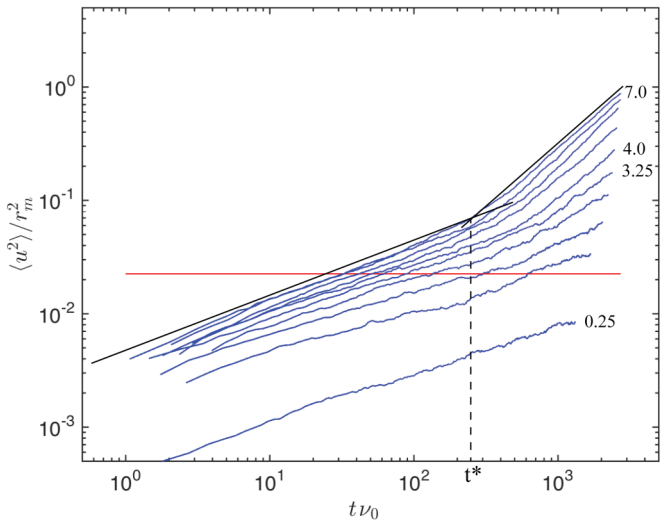


FIG. 14. Mean-square displacement $\langle u^2\rangle/r_m^2$ (MSD) of a particle array on an unduloid, with $r_m$ the equilibrium spacing of the ordered lattice. The dimensionless inverse potential depth $k_BT/\epsilon$ is increased in multiples of 0.75 as indicated for some curves. The horizontal red solid line is the late-time MSD of the particles on a flat Lennard-Jones hexagonal lattice at the melting point. The upper black solid line has a slope for an MSD proportional to $t$ (diffusion) and the lower black solid line has a slope for an MSD proportional to $t^\alpha$ with $\alpha \simeq 0.5$ (subdiffusion). For $k_BT/\epsilon = 7$ subdiffusion crosses over to diffusion at a scale $t^*$ determined by the intersection of these black lines.

that at the melting transition $\langle u^2\rangle/r_m^2 \simeq 0.021$ [27], which can be viewed as a version of the Lindemann melting criterion. For our case however, the late-time value of $\langle u^2\rangle/r_m^2$ for $k_BT/\epsilon = 3.25$ was about twice larger. This relative stabilization of an ordered array on a cylindrical surface as opposed to a planar surface is attributed to the restriction on thermal fluctuations imposed by the cylindrical geometry.

Next, we repeated the simulations on an unduloid surface with results shown in Fig. 14.

The MSD-time plots no longer saturate at late times, even for the smallest value of $k_BT/\epsilon$. Instead, for larger $k_BT/\epsilon$ the MSD-time plots show a change in the slope $\alpha$ on a log-log plot from about 0.5 (subdiffusion) to about 1.0 (diffusion). The crossover for the case of $k_BT/\epsilon = 7$ takes place at time $t^*$ obtained from the intersection of the two solid lines shown in Fig. 14. As $k_BT/\epsilon$ is reduced, the crossover time $t^*$ shifts to higher values and for $k_BT/\epsilon$ less than about 1.75 we only observe subdiffusion.

If an MSD-time plot has the power-law form $\langle u^2(t)\rangle \propto t^\alpha$ then that translates in the frequency domain to $\langle u^2(\omega)\rangle \propto 1/|\omega|^{1+\alpha}$. The fluctuation-dissipation theorem states that $\langle u^2(\omega)\rangle = (2k_BT/\omega)\mathrm{Im}[1/G(\omega)]$ for thermally equilibrated particle systems, where $G(\omega)$ is the frequency-dependent complex dynamic modulus of the particle system. For a Newtonian fluid $\mathrm{Im}[1/G(\omega)] \propto 1/\omega$ while for an ordered solids, $\mathrm{Im}[1/G(\omega)] \propto \omega$ at low frequencies. Materials that, as in the present case, have a low-frequency complex modulus $G(\omega) \propto \omega^\alpha$ with an exponent $\alpha$ that lies in between these two limits are viscoelastic. This means that, though they are not simple liquids, when subject to a constant shearing stress they undergo a steadily increasing shear deformation. When applied to the ATV capsid, this means that the steady shear stress generated by the tail sections can produce large-scale deformations of the capsid shape for values of $k_BT/\epsilon$ that are well below the melting point of the cylindrical sections.

The mechanism underlying the viscoelasticity at small $k_BT/\epsilon$ is the stress-induced motion of the defects arrays present in the ground state. We saw that particle arrays on both unduloid and spherical surfaces contain unbound dislocations and scars. Two-dimensional materials with free dislocations and/or mobile grain boundaries indeed are known to have the flow properties of viscoelastic materials [28].

The late-time MSDs of unduloid, sphere, and cylinder were all fitted to straight lines. These slopes were then averaged over six different KMC simulations for each value of $k_BT/\epsilon$ to arrive at the effective diffusion coefficients shown in Fig. 15. The single-particle diffusion coefficients of particle arrays covering either an unduloid or a sphere lack the onset feature shown clearly by the diffusion coefficients of the cylindrical surface. The obvious interpretation is that the intrinsic defects that are present in the case of the unduloid and the sphere, but not in the case of the cylinder, prevent freezing. The diffusion coefficients for the unduloid case lie, in general, between those of the cylinder and the sphere.

We propose that ATV tail growth is enabled by transport of particles from the main body of the capsid to the roots of the growing tails where they are absorbed into the tails. It still is possible that particle transport at the minimum cross section of the unduloid is significantly less than the

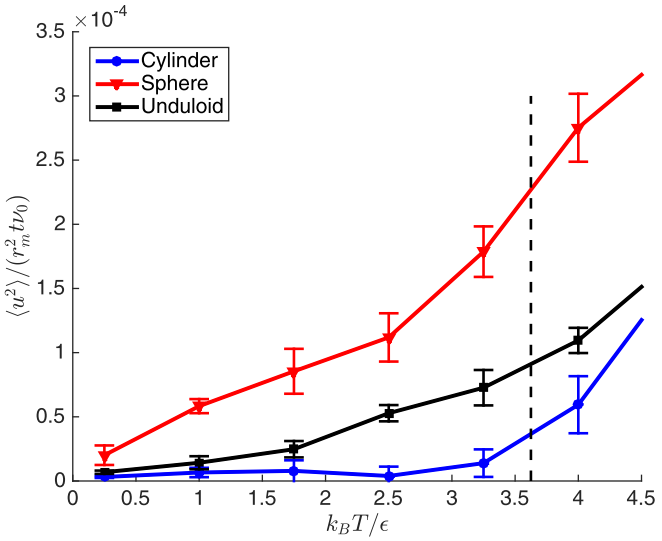


FIG. 15. Average late-time slope of the MSD vs time as a function of $k_BT/\epsilon$ with $\epsilon$ the LJ binding energy. The average slope together with its standard deviation (error bars) were obtained from six different KMC analyses per $k_BT/\epsilon$ and per geometry. Black line: unduloid. Red line: sphere. Blue line: cylinder. Vertical dashed line: estimated melting point for the cylinder.

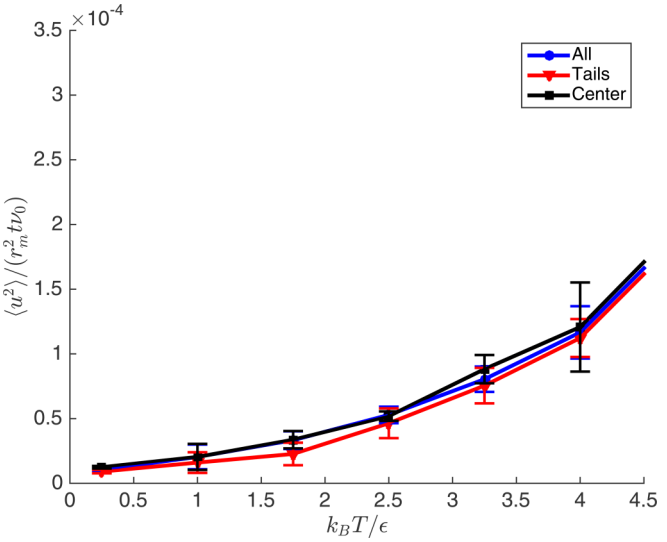


FIG. 17. Average MSD slope vs time as a function of $k_BT/\epsilon$ for an unduloid with periodic boundary conditions. Black line: MSD of particles in the center (central third). Red line: MSD of particles in the tails (initial and final thirds). Blue line: all particles.

one at the maximum cross section, in which case tail growth would be suppressed. In order to check for nonuniformity of the MSDs, we repeated the previous simulations using periodic boundary conditions so transport in the neck regions is not suppressed (previous simulations were carried out with fixed boundary conditions at the necks). An example of a simulation result with periodic boundary conditions is shown in Fig. 16 for $k_BT/\epsilon = 2.5$. Figure 17 shows that MSDs computed using periodic boundary conditions are, within error bars, the same in the tail and in the central regions. Thermal production of defects in the neck region is comparable to that in the main body except that there is an excess of isolated heptamers. This is consistent with the fact that the elastic energy of sevenfold disclinations is minimized in regions of negative Gauss curvature [20]. Equilibrated particle arrays placed on surfaces with negative Gauss curvature have indeed been observed to carry a distribution of sevenfold disclination defect [22].

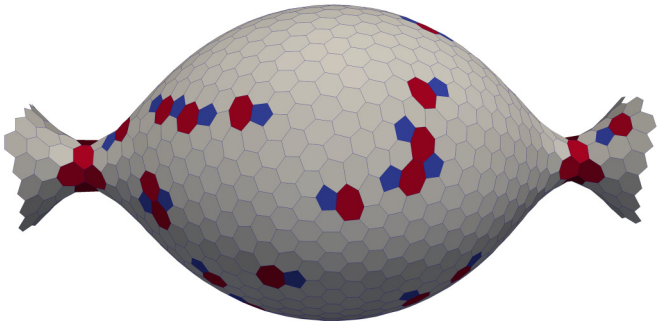

FIG. 16. Late-time snapshot of a simulation with periodic boundary conditions at $k_BT/\epsilon = 2.5$

In order to estimate the transport rates of protein oligomers on ATV, we use the fact that the self-diffusion coefficient $D$ of particles as part of an array must be proportional to the diffusion coefficient of isolated particles. Physical self-diffusion coefficients can thus be obtained by dividing numerically computed self-diffusion constants by the bare diffusion coefficient $D_0 \propto a^2\nu_0$ and then multiplying with experimentally measured single-particle diffusion coefficients under appropriate conditions. As an example, for $k_BT/\epsilon = 2.5$, which is well below the melting point for the cylinder, the effective diffusion coefficient obtained from the late-time (so with $t > t^*$) MSD-time slope is $0.5 \times 10^{-4}$ (our units). Dividing by the single-particle diffusion coefficient $D_0 \simeq 2.7 \times 10^{-3}$ in our units and multiplying by the diffusion coefficient of a particle in water with the size of ATV capsid oligomer (about $10^{-6}\,\mathrm{cm}^2/\mathrm{s}$) leads to an effective diffusion coefficient of about $2 \times 10^{-8}\,\mathrm{cm}^2/\mathrm{s}$. If the size of the ATV virus is estimated to be 100 nm (Fig. 2), then a capsid oligomer could diffuse over the length of the ATV body in $\approx 1.25 \times 10^{-1}$s.

### D. Tension fluctuations

The final step was to examine the properties of particle arrays under tension. Recall that, according to continuum theory, tension across the surface of closed shells is generated by a pressure difference across the surface of the shell. The first aim is to verify that for discrete arrays the same is true and that the Laplace law is obeyed. Also, according to Laplace's law, a local tension reduction must be compensated by an increase in the local mean curvature, thus a bulge formation. If the stretching along the bulge produces a further decrease of the tension then the curvature will increase even further, eventually leading to an aneurysm-type rupture. Therefore, if there is a tension reduction along the scars and defects or

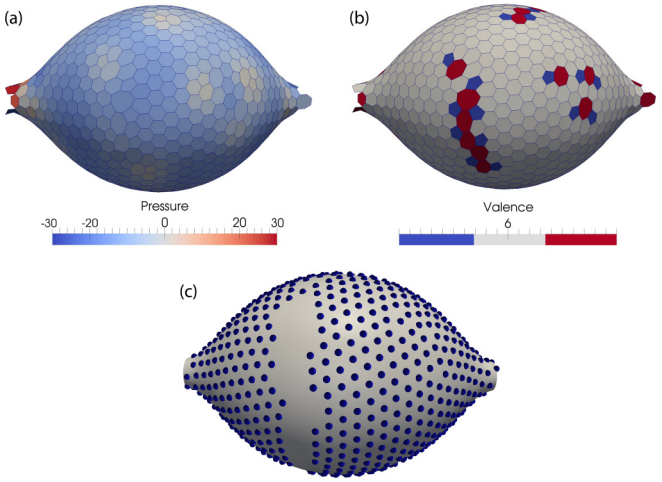


FIG. 18. (a) Averaged normal forces per unit area computed with a particle array under tension on an unduloid. The system was under an applied tension of approximately 5% while $k_BT/\epsilon = 0.05$. Note that there are significant pressure variations. (b) Corresponding defect array. Note that there is some correlation between low-pressure regions and heptamers. (c) Capsid rupture under a larger applied tension of $\approx 6\%$.

any other source of tension variation, this could lead to an aneurysm-type mechanical instability.

We performed MC simulations of tense particle arrays, using as our starting configuration a representative particle array obtained in the MC analyses presented in Sec. III B [see Fig. 18(b)]. The initial array was typically in a state of slight compression. Next, we instantaneously decreased the equilibrium distance $r_m$ of the LJ potential by $\delta r$, which places the system under tension corresponding to a strain of $\delta r/r_m$. We then carried out MC simulations to allow the particle arrays to relax towards equilibrium. For $k_BT/\epsilon = 0.05$, the array did not rupture for stretching strains $\delta r/r_m$ below about 0.05 while for stretching strains of 0.06, the system did rupture, as shown in Fig. 18(c). The rupture strain decreased for lower values of $\epsilon$.

We then computed the forces exerted on each particle and added the component of each force in the direction normal to the surface. Subsequently, we divided the total normal force component by the area of the Wigner-Seitz cell centered at each particle and calculated a site pressure $\Pi$ at the position of that particle. We then averaged $\Pi$ in space over the ring of nearest neighbors and in time over 30 MC steps equally spaced over the last ten percent of the duration of the simulation. We computed the local in-plane stretching tension $\tau_i$ in a similar fashion. The local value $\tau_i$ was found to be within a factor two of the Laplace law value $2\Pi H$, with $H$ the mean curvature. The discrepancy is attributed to the discreteness of the underlying mesh and the discreteness of the particle array, which limits the applicability of continuum theory.

Figure 18(a) shows the pressure distribution for an imposed stretching strain of 0.049. About 96% of the surface was under tension. If the imposed tension is decreased, then the fraction of the surface under tension decreases further. The pressure scale is shown in units of $0.043\epsilon/r_m^3$, with an average pressure of about ten units. For $\epsilon = 5k_BT$, $T = 300$ K, and $r_m = 6$ nm, the average pressure would be about 40 kPa, close to the pressure we estimated as relevant for ATV before tail growth. The standard deviation of the pressure fluctuations—approximately 24 kPa—is comparable to the mean. The pressure variations that can be seen in Fig. 18(a) are, at least in part, correlated with the distribution of defects in Fig. 18(b), though scars are not lines of low tension.

## IV. SUMMARY

We propose a model for the capsid of the ATV archaeal virus as a viscoelastic membrane under tension generated by genomic osmotic pressure. According to continuum theory, the capsid has the shape of a surface of constant mean curvature, specifically that of an unduloid. Growth of the central filament reduces the capsid volume, compresses the genome and increases the osmotic pressure. The increase in osmotic pressure suggests that one of the roles of the ATV shape change could be to prime the capsid for release of the genome through the tails after the virus has attached itself to a host cell.

In order to further study the mechanisms underlying the tail growth, we performed simulations of particle arrays covering an unduloid. We found that for radial interaction potentials, the CK spiral construction is unstable against the formation of scars and other defects that appear to be an intrinsic feature of the thermodynamic ground state of large particle arrays on an unduloid, just as they are on spherical surfaces. Because of the presence of these defects, the body of the capsid remains viscoelastic at capsomer-capsomer interaction strengths well above the onset point of positional order on the cylindrical tail sections. This viscoelasticity would allow for the large observed shape changes.

Is the capsomer transport rate sufficiently high for the tail growth of an ATV virus? For $k_BT/\epsilon = 2.5$ the effective late-time self-diffusion coefficient is in the range of $2 \times 10^{-8}$ cm$^2$/s. If one assumes that tail growth requires a supply of about ten circumferential oligomers for the growth of one oligomer length of tail, this leads to a tail extension rate of about 300 nm/minute.

The most serious concern we encountered with the proposed model is that of rupture generated by tension nonuniformity. The range of imposed tension strains over which the particle array is fully under tension yet does not rupture is small. Moreover, inside this range, the surface is subject to large-scale pressure fluctuations that may lead to mechanical instability of the aneurysm type. We believe, but have not yet shown, that anisotropic pair potentials could increase the stability range and suppress the fluctuations by organization of particles into polymeric linear arrays, e.g., into spirals as shown in Ref. [29] for a polyelectrolyte on a spherical surface. When wound around the unduloid according to the CK spiral construction these polymers might suppress rupture and aneurysm instabilities. In the presence of a sufficient level of thermal fluctuations, the protein chains still would be able to slide past each other so the shear elastic modulus would be zero for longitudinal sliding transport while the shear modulus in the transverse direction would remain finite. We hope to address these questions in future work.

If the proposed description does apply, then ATV capsids would be very interesting model systems from the viewpoint of the statistical physics of particle arrays on curved surfaces. While scar-type defects of particle arrays covering spheres have been discussed in the colloid literature, they have not (yet) been seen for large spherical viral shells. In the proposed description, scars are an intrinsic feature of the capsid of ATV viruses and play a functional role in maintaining the viscoelasticity of the capsids that allow for the growth of the tails, even when the capsomers have relatively high binding energies.

Experimental tests of the proposed model should be possible. The level of resolution of current electron microscopy should be sufficient to confirm (or disprove) the presence of scars along the capsids of ATVs. The 100 nm ATV capsids also may just be large enough for tracking fluorescently labeled capsid proteins that could measure MSD-time plots.

An interesting challenge for the proposed model is the fact that in the early stage of tail growth the capsid does not appear to be a surface of constant mean curvature. We proposed earlier that this may be due to nonuniformity of the osmotic pressure. In fact, a variety of puzzling capsid shapes have been reported for other archaeal viral capsids that—at least at first sight—also do not resemble surfaces of revolution of constant mean curvature (e.g., see Fig. 1). It is not known if that is due to some form of internal structure or to pressure nonuniformity.

Is the tense-surface description of viscoelastic or fluid capsids restricted to archaeal viruses? Observational bias towards ordered viral capsids whose atomic structure can be resolved by x-ray diffraction may have obscured the possibility that viral capsids could be in a quasifluid state. Significant levels of fluidity, structural disorder, and pleomorphism have been reported for the archaeal HRPV virus [30] and HRPV itself may be related to the *Bunyaviridae* family of nonarchaeal viruses. Members of the *Bunyaviridae* family indeed appear to be characterized by pleomorphism [31].

## ACKNOWLEDGMENTS

We would like to acknowledge important discussions with Alexander Grosberg, Martin Lawrence, and Alex Levine as well as support from the NSF under DMR Grant No. 1309423.

## APPENDIX A: UNDULOID

The unduloid is a surface of revolution with a constant mean curvature. This surface arises from the minimization of surface area subject to the constraint of fixed volume. The quantity to be minimized in such a case is

$$\int_0^L \{y(x)\sqrt{1+[dy(x)/dx]^2} - \lambda y(x)^2\}dx, \tag{A1}$$

where $y(x)$ is the curve that is rotated about the $x$ axis and $\lambda$ is the Lagrange multiplier corresponding to the constant volume constraint. The quantity $\lambda$ can also be seen as representing the internal pressure of an enclosed isotropic substance. Standard methods lead to the following relation:

$$\frac{y(x)}{\sqrt{1+[dy(x)/dx]^2}} - \lambda y(x)^2 = C, \tag{A2}$$

where $C$ is a constant. This equation is readily manipulated into the form

$$\frac{dy(x)}{dx} = \pm\frac{\sqrt{y(x)^2 - [C+\lambda y(x)^2]^2}}{\lambda y(x)^2 + C}, \tag{A3}$$

which leads us to the quadratures solutions

$$\int \frac{\lambda y^2 + C}{\sqrt{y^2 - (\lambda y^2 + C)^2}} = \pm\int dx. \tag{A4}$$

The left-hand side of (A4) can be rewritten in the following form

$$\int \frac{y^2 + r_1 r_2}{\sqrt{(r_1 - y)(y - r_2)(y + r_1)(y + r_2)}}, \tag{A5}$$

where

$$r_1 = \frac{1}{2}\left[\frac{1}{\lambda} + \sqrt{\frac{1}{\lambda^2} - 4\frac{C}{\lambda}}\right]; \tag{A6}$$

$$r_2 = \frac{1}{2}\left[\frac{1}{\lambda} - \sqrt{\frac{1}{\lambda^2} - 4\frac{C}{\lambda}}\right]. \tag{A7}$$

The integral in (A5) can be expressed in terms of elliptic integrals. The solutions of interest arise from a positive discriminant in (A6) and (A7), leading to real values for the roots $r_1$ and $r_2$.

Taking the Lagrange multiplier $\lambda$ to be positive, we can distinguish between two cases, corresponding to two possible signs of the combination $C/\lambda$. If $C/\lambda$ is positive, which is the condition that is relevant to the work reported here, then the graph on the left-hand side of Fig. 19 applies.

The two red curves in that graph correspond to $\pm(\lambda y^2 + C)$. The straight line is at 45° with respect to the two axes. According to (A2), we must have $y \geqslant C + \lambda y^2$. The equality in this expression holds if $dy(x)/dx = 0$. Furthermore, we restrict $y(x)$ to be positive, as it corresponds to the radius of the surface of revolution. The solution to the minimization equation must therefore lie in the portion of the upper quadrant of the left-hand graph for which the black line lies above the upper red parabola. In this case, both $r_1$ and $r_2$ are greater than zero and correspond to the two points of intersection of

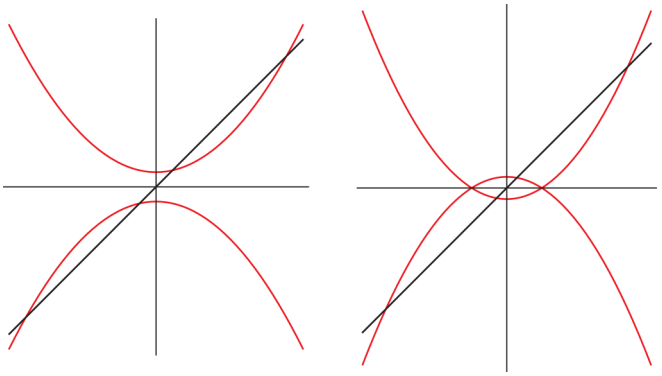

FIG. 19. The two possibilities for the parameters in the quadrature equations leading to a minimum surface of revolution with fixed volume. The case illustrated on the left relates to the work reported here.

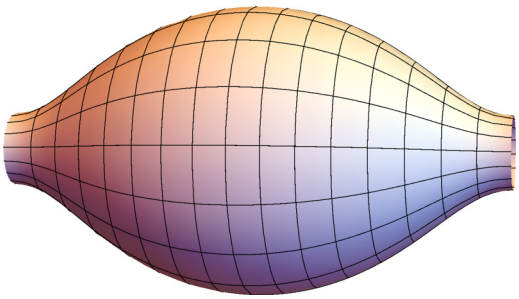

FIG. 20. A minimizing surface corresponding to the conditions illustrated on the left-hand side of Fig. 19.

the black line with the upper parabola. At those points the derivative $dy(x)/dx$ vanishes.

We can go further and scale out the constant $\sqrt{r_1 r_2}$. Then, the only remaining parameter determining the surface of revolution is, say, the rescaled smaller root, $r_1/\sqrt{r_1 r_2}$. The other scaled root is its inverse. A surface corresponding to these conditions is shown in Fig. 20.

## APPENDIX B: PARTICLE PLACING ON A SURFACE OF REVOLUTION

In this section we discuss a strategy to place spherical particles of the same diameter (representing protein capsomers) on a surface of revolution so that the particles are (approximately) evenly distributed. As described in the previous section, let a surface of revolution be described by the function $y(x)$, where $x$ represents the distance along the axis of symmetry (Fig. 21.) A simple strategy to place the particles on this surface would be to wrap them along helices. In order to evenly distribute particles on a noncylindrical surface the pitch of the helices must change as they wrap around the surface.

Let us consider $m$ helices winding around the surface (as shown schematically in Fig. 21). We assume that the helices are closely spaced so that the distance between helices measured along the surface may be approximated by their straight line distance. Let us consider two adjacent helices 1 and 2 as shown in Fig. 21 and choose two points $A$ and $B$ on each helix, respectively, at the same meridional angle $\theta$. The distance

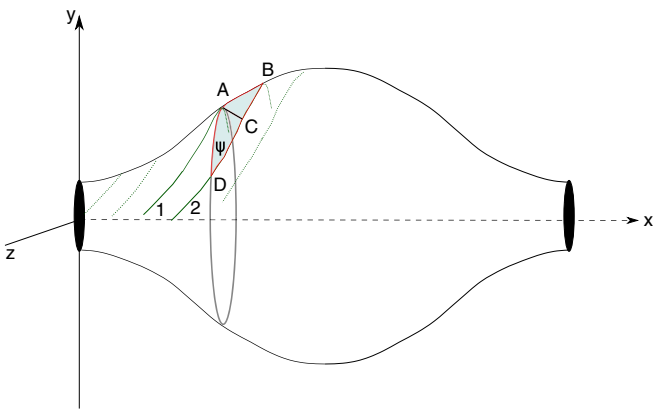


FIG. 21. Schematic of helices on a surface of revolution.

$|AB|$ approximated by the arc length is $\sqrt{1+(dy/dx)^2}dx$. Similarly, the distance between points $A$ and $D$ placed at the same $x$ is $y(d\theta/dx)dx$. Consequently for the right triangle $DAB$, the angle $\psi$ ($\measuredangle ADB$) is given by

$$\sin\psi = \frac{\sqrt{1+(dy/dx)^2}}{\sqrt{1+(dy/dx)^2+y^2(d\theta/dx)^2}}. \tag{B1}$$

The perpendicular distance $d$ between the helices is given by

$$d = |AC| = |AD|\ \sin\psi. \tag{B2}$$

If the helices are to be evenly spaced everywhere, $d$ must be a fixed constant for the surface. Moreover, for the $m$ helices evenly spaced at every cross section, it is clear that $|AD|$ is proportional to $y$, since $m|AD| = 2\pi y$. This observation together with Eq. (B2) implies

$$\frac{y\sqrt{1+(dy/dx)^2}}{\sqrt{1+(dy/dx)^2+y^2(d\theta/dx)^2}} = r_2, \tag{B3}$$

where $r_2$ is an arbitrary constant. If the helices are assumed to arise perpendicularly at $x=0$, i.e., $d\theta/dx(0)=0$, then it is clear from (B3) that $r_2$ represents the radius of the surface of revolution at $x=0$. We solve this (first-order) differential equation for $\theta(x)$ by choosing an initial condition $\theta(0)=\theta_0$ to distinguish each of the $m$ helices. Each helix is then described by the parametric equation

$$\mathbf{r}(x) = x\mathbf{i} + y(x)\cos[\theta(x)]\mathbf{j} + y(x)\sin[\theta(x)]\mathbf{k}. \tag{B4}$$

We note that while (B3) may be solved numerically for an arbitrary surface of revolution, for the cases considered here—cylinder, sphere, and unduloid—it is possible to solve the equation in closed form. For a cylinder of radius $r$, defined by the equation $y(x)=r$, the construction is trivial. We now summarize the results for the unduloid and the sphere.

### 1. Helices on an unduloid

Making use of (A5), we can rewrite (A4) as

$$\frac{dy}{dx} = \pm\frac{\sqrt{(r_1^2-y^2)(y^2-r_2^2)}}{y^2+r_1 r_2}. \tag{B5}$$

Using (B5) in (B3) and writing $\theta$ as a function of $y$, we obtain

$$\frac{d\theta}{dy} = \frac{r_1+r_2}{r_2}\frac{1}{\sqrt{r_1^2-y^2}}, \tag{B6}$$

which can be integrated to yield

$$\theta(y) = \frac{r_1+r_2}{r_2}\arcsin(y/r_1)+\theta_0. \tag{B7}$$

### 2. Helices on a sphere

In the case of the sphere, it is more convenient to choose the azimuthal angle $\phi$ to be the independent variable, instead of $x$. The transformation between $\phi$ and $x$ is given by $x = 1-\cos\phi$, while the surface of the sphere, as a surface of revolution, is defined by $y(\phi) := \sin\phi$.

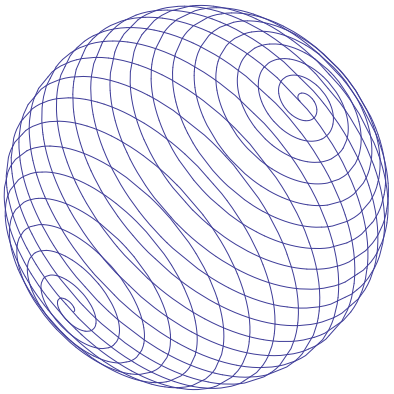

FIG. 22. Helix uniformly covering the sphere.

Rewriting (B3) in terms of $\phi$, we obtain

$$\frac{d\theta}{d\phi} = \pm\frac{\sqrt{\sin^2\phi - \sin^2\phi_o}}{\sin\phi\,\sin\phi_o}, \tag{B8}$$

where, for convenience, we write $r_2 = \sin\phi_0$. This equation can be integrated to yield

$$\theta(\phi) = \csc\phi_0\left[-\sqrt{-\sin^2\phi_0}\tanh^{-1}\left(\frac{\cos\phi\sqrt{\cos(2\phi)-1}}{\sqrt{\cos(2\phi_0)-\cos(2\phi)}}\right)\right.$$
$$\left. + i\,\ln(\sqrt{\cos(2\phi_0)-\cos(2\phi)} + i\sqrt{2}\cos\phi)\right] + \theta_0. \tag{B9}$$

By suitably choosing $\phi_0$, we can cover the surface of a sphere using just one helix as shown in Fig. 22 or using five helices as shown in Fig. 23 to obtain a CK $T = 7$ icosahedral structure.

## APPENDIX C: METROPOLIS MONTE CARLO ALGORITHM

We use the Metropolis Monte Carlo method to calculate the particle positions on an underlying fixed grid corresponding to the particle ground state (Sec. III B). The algorithm proceeds as follows.

(1) (**Particle move**) A particle is chosen at random and moved to a node in its first neighbors ring. The node to which the particle moves is also chosen at random and the set of possible moves includes the particle's original location, i.e., the particle may be left in place. The particles move on a fine underlying triangular lattice with mesh size $a$. We choose $a = r_m/16$, where $r_m$ is the particle equilibrium distance (Fig. 24).

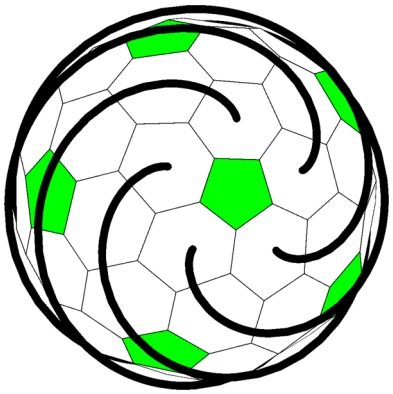

FIG. 23. Five helices covering a sphere. The $T = 7$ construction is recovered when they are decorated with particles.

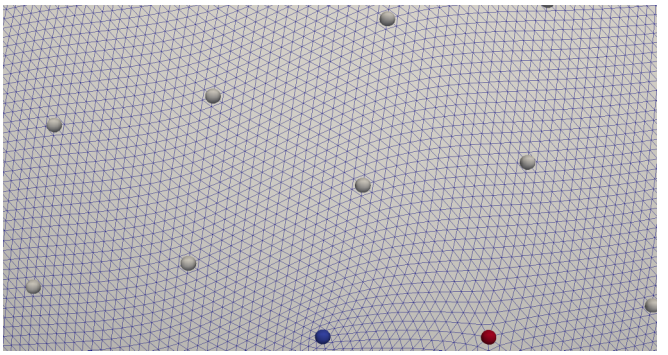

FIG. 24. A zoomed-in view of the underlying lattice on which the particles move.

(2) (**System energy**) For each move of a particle $k$, the new energy of the entire system $E_{\text{new},k}$ and change in energy $\Delta E_k = E_{\text{new},k} - E_{\text{old},k}$ are computed. $E_{\text{new},k}$ and $\Delta E_k$ are computed after only particle $k$ has moved.

(3) (**Move acceptance or rejection**) If for particle $k$, either $\Delta E_k < 0$ or $\eta < \exp(-\Delta E_k/\tilde{T})$ the move is accepted, otherwise it is rejected. Here $\tilde{T} = k_B T$ and $\eta \in [0,1]$ is a randomly chosen number.

(4) (**Annealing at constant temperature**) Steps 1 through 3 are repeated for each of the $N$ particles of the system.

(5) (**Temperature schedule**) The pseudo temperature $\tilde{T}$ is lowered according to $\tilde{T}_{t+1} = \alpha\tilde{T}_t$ and steps 1 through 4 are repeated, i.e., steps 1 through 4 are carried out only once at constant $\tilde{T}$. $\alpha = \left(\frac{\tilde{T}_{\text{final}}}{\tilde{T}_{\text{initial}}}\right)^{1/M}$ where $M$ is the number of Metropolis Monte Carlo steps at different temperatures.

The steps outlined in the foregoing are summarized in Algorithm 1.

**Algorithm 1** Metropolis Monte Carlo Algorithm

Consider a system of $N$ particles $k$ moving on an underlying fine lattice (Fig. 24). Each node on the finer lattice is denoted by $n$ and the subset of nodes in the first ring of neighbors of particle $k$ is denoted by $\Omega_k$. $\Omega_k$ includes the node at which particle $k$ is. The system initial scaled temperature is $\tilde{T}_{\text{init}}$ and the final scaled temperature is $\tilde{T}_{\text{final}}$. We define $\alpha = \left(\frac{\tilde{T}_{\text{final}}}{\tilde{T}_{\text{initial}}}\right)^{1/M}$

**For** $t \in \{1,2,\cdots,M\}$ **do** ▷ Decrease temperature
  $\tilde{T}_t = \alpha\tilde{T}_{t-1}$
  **For** $k \in \{1,2,\cdots,N\}$ **do** ▷Iterate over particles
    Randomly choose a particle $k$.
    Randomly select a node $\bar{n} \in \Omega_k$
    Move particle $k$ to $\bar{n}$. We denote this state $S_k$.
    $p_k \leftarrow e^{-\Delta E_k/\tilde{T}_t}$
    $\eta \leftarrow$ RAND[0,1]
    **If** $\Delta E_k < 0 \vee \eta < p_k$ **then** ▷Accept criterion
      Accept $S_k$
    **end if**
  **end for**
**end for**

In order to calibrate the parameters governing the Metropolis Monte Carlo algorithm, i.e., initial and final temperatures and rate of temperature decay, we first compute the minimum energy configuration for known cases, i.e., the particle configuration on a cylinder (Fig. 9) and on a small icosahedral geometry corresponding to a $T = 7$ virus (Appendix E). Subsequently, we apply the same minimization algorithm to the unknown unduloid case. Since the minimum energy particle configuration is likely to be nonunique, we repeat the analyses several times to ensure that the computed configuration is representative of the particles minimum energy states.

In all the simulations reported in Sec. III B and Appendix E, we set $\tilde{T}_{\text{initial}} = 5$, $\tilde{T}_{\text{final}} = 5 \times 10^{-3}$ and the total number of Monte Carlo steps is equal to 15000. Each complete Monte Carlo step corresponds to $N$ attempted particle moves, where $N \approx 1000$ for the cylinder, sphere, and unduloid geometries.

## APPENDIX D: KINETIC MONTE CARLO METHOD

For the diffusive transport studies discussed in Sec. III C, we use the null process method [32], a version of the kinetic Monte Carlo method that is based on the familiar $n$-fold method [33]. This method was originally introduced in the context of large reaction-diffusion systems with a fixed number of processes. According to the null process method, the system is divided into a number of cells or subsystems and a modified version of the $n$-fold algorithm is applied to each subsystem. To achieve synchrony, null events are introduced. In a subsystem, a null event represents no change to the subsystem but retains a finite probability of being selected. However, the algorithm is designed such that there is at least one subsystem in which the null event never occurs. Consequently, the method still retains the rejection-free paradigm of the $n$-fold scheme. A parallel generalization of this scheme has been developed in Ref. [34].

To apply the method to the problem at hand, we divide the system of $N$ particles into subsystems each with one particle. Each particle (indexed by $k \in \{1,2,\ldots,N\}$) is randomly perturbed while holding the others fixed. The rate of every such a transition is computed according to

$$r_k = \nu_o e^{-\Delta E_k/\tilde{T}}, \quad k \in \{1,2,\ldots,N\},$$

where $\nu_0$ is a constant that determines the time scale. After $r_k$ is computed for all particles, each move is accepted with probability $p_k = r_k/r_{\max}$, where $r_{\max}$ is the maximum rate:

$$r_{\max} = \max_{k\in\{1,2,\cdots,N\}}\{r_k\}.$$

The rejection probability of $1 - p_k$ is equal to the probability of acceptance of the null event. Finally, time increments are chosen according to a Poisson distribution:

$$\Delta t = -\frac{\ln \xi}{r_{\max}},$$

where $\xi \in (0,1)$ is a random number from a uniform distribution. A pseudocode for this method is summarized in Algorithm 2.

**Algorithm 2** Kinetic Monte Carlo Algorithm

Divide the system of $N$ particles into $N$ subsystems with one particle each.
For every time step do:
**For** $k \in \{1,2,\cdots,N\}$ **do**
  Randomly perturb particle $k$ while holding others fixed. Call this state $S_k$.
  Compute rate $r_k$ for such a transition to $S_k$ according to:
$$r_k \leftarrow \nu_o e^{-\Delta E_k/\tilde{T}},$$
where $\nu_0$ is a constant scaling for time.
**end for**
$r_{\max} \leftarrow \max_{k\in\{1,2,\cdots,N\}}\{r_k\}$ ▷ Compute max. rate
**For** $k \in \{1,2,\cdots,N\}$ **do**
  $p_k \leftarrow r_k/r_{\max}$
  $\eta \leftarrow \text{RAND}(0,1)$
  **If** $p_k > \eta$ **then** ▷ Accept $S_k$ with probability $p_k$
    Accept $S_k$
  **end if**
**end for**
$\xi \leftarrow \text{RAND}(0,1)$ ▷ $\Delta t$ from Poisson distribution
$\Delta t \leftarrow -\frac{\ln \xi}{r_{\max}}$

### Tests

We verified our algorithm with two of the tests discussed in Ref. [34]: (i) diffusion of particles on a lattice without interactions and with absorbing boundary conditions; and (ii) diffusion of identical particles with annihilation interaction given by the reaction $A + A \to 0$.

For the first case, we use a two-dimensional square lattice with 1229 noninteracting particles subjected to the condition that any particle reaching the boundary is absorbed (that is, removed). The time dependence of the concentration is plotted in Fig. 25 and agrees well with the theoretical prediction reported in Ref. [34].

The second test case involves identical interacting particles ($A$) on a square lattice. The interaction is governed by the reaction $A + A \to 0$, that is, two particles within a (prescribed) threshold interaction radius annihilate each other. The time-dependent concentration (with 961 particles at time

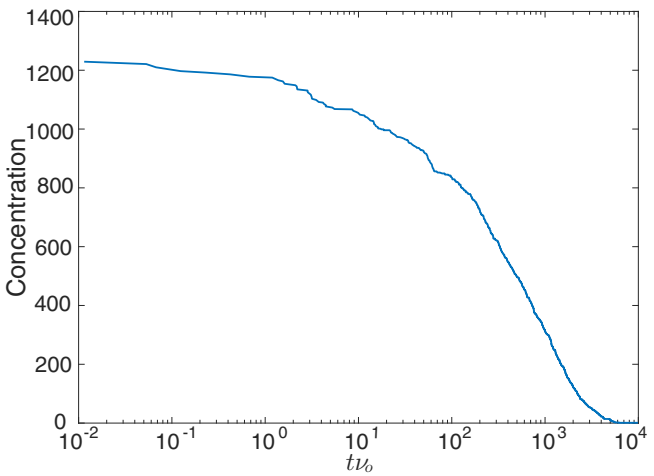


FIG. 25. Concentration vs time for diffusion problem with no particle interactions and absorbing boundary conditions.

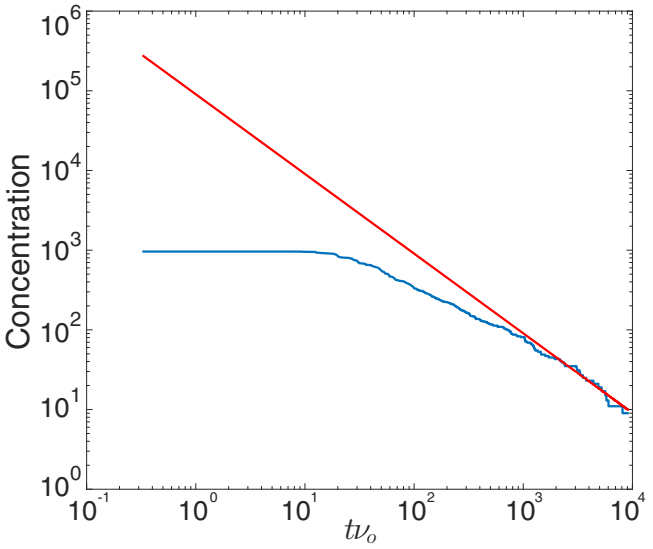


FIG. 26. Concentration vs time for diffusion problem with annihilation reaction A+A → 0

$t = 0$) is shown in Fig. 26. The asymptote for large $t$ agrees with a $1/t$ dependence for the concentration and it is in agreement with the theoretical prediction [34].

## APPENDIX E: ANNEALING OF $T = 7$ STRUCTURE

We additionally validate the Monte Carlo annealing procedure used in Sec. III B and presented in Appendix C for small spherical viruses, such as $T = 7$. The initial particles' distribution corresponding to the capsomers of a $T = 7$ structure is constructed according to the procedure described in Appendix B2 [Fig. 27(a)]. Subsequently, the Monte Carlo algorithm presented in Appendix C is applied, maintaining the same analysis setup (e.g., initial temperature, rate of temperature decay, depth of the Lennard-Jones potential) as for the unduloid, cylinder, and sphere cases. Following the initial temperature increase, heptamers are formed as the energy of the system increases [Fig. 27(b)]. As the temperature is gradually lowered, the ground state corresponding to a $T = 7$ structure is recovered [Fig. 27(c)]. Due to the motion during the annealing procedure, the particles in the final configuration do not occupy the same positions as at the beginning, but the $T = 7$ structure is rotated as shown by the superimposed initial and final capsomer outlines [Fig. 27(c)]. This result verifies that, using the adopted procedure, the particles undergo large enough displacements (i.e., do not necessarily fall back into their original positions) and explore other possible configurations.

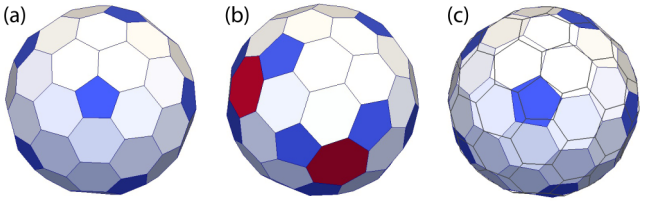


FIG. 27. Initial, intermediate (at 1100 Monte Carlo steps) and final capsomers configuration during Monte Carlo annealing of a $T = 7$ virus structure. Due to the particles' motion during the annealing procedure, the initial and final capsomers configurations are rotated with respect to each other.


[1] W. Roos, R. Bruinsma, and G. Wuite, Nat. Phys. **6**, 733 (2010).
[2] J. Lidmar, L. Mirny, and D. R. Nelson, Phys. Rev. E **68**, 051910 (2003).
[3] D. L. Caspar and A. Klug, in *Cold Spring Harbor Symposia on Quantitative Biology*, Vol. 27 (Cold Spring Harbor Laboratory Press, Cold Spring Harbor, 1962), pp. 1–24.
[4] R. Zandi, P. van der Schoot, D. Reguera, W. Kegel, and H. Reiss, Biophys. J. **90**, 1939 (2006).
[5] T. T. Nguyen, R. F. Bruinsma, and W. M. Gelbart, Phys. Rev. E **72**, 051923 (2005).
[6] C. R. Woese and G. E. Fox, Proc. Natl. Acad. Sci. USA **74**, 5088 (1977).
[7] M. Pina, A. Bize, P. Forterre, and D. Prangishvili, FEMS Microbiol. Rev. **35**, 1035 (2011).
[8] D. Prangishvili, P. Forterre, and R. Garrett, Nat. Rev. Microbiol. **4**, 837 (2006).
[9] M. Häring, G. Vestergaard, R. Rachel, L. Chen, R. A. Garrett, and D. Prangishvili, Nature (London) **436**, 1101 (2005).
[10] M. Häring, R. Rachel, X. Peng, R. A. Garrett, and D. Prangishvili, J. Virol. **79**, 9904 (2005).
[11] D. Prangishvili, G. Vestergaard, M. Häring, R. Aramayo, T. Basta, R. Rachel, and R. Garrett, J. Mol. Biol. **359**, 1203 (2006).
[12] H. H. Strey, V. A. Parsegian, and R. Podgornik, Phys. Rev. Lett. **78**, 895 (1997).
[13] W. Gelbart, R. Bruinsma, P. Pincus, and V. Parsegian, Phys. Today **53**, 38 (2000).
[14] W. M. Gelbart and C. M. Knobler, Science **323**, 1682 (2009).
[15] P.-G. De Gennes, F. Brochard-Wyart, and D. Quéré, *Capillarity and Wetting Phenomena: Drops, Bubbles, Pearls, Waves* (Springer Science & Business Media, Berlin, 2013).
[16] M. Hadzhilazova, I. Mladenov, and J. Oprea, Arch. Math. Brno **43**, 417 (2007).
[17] C. Delaunay, J. Math. Pures et Appliquées **6**, 309 (1841).
[18] J. Theriot, Traffic **1**, 19 (2000).
[19] R. Zandi, D. Reguera, R. Bruinsma, W. Gelbart, and J. Rudnick, Proc. Natl. Acad. Sci. USA **101**, 15556 (2004).
[20] H. S. Seung and D. R. Nelson, Phys. Rev. A **38**, 1005 (1988).
[21] V. Vitelli, J. Lucks, and D. Nelson, Proc. Natl. Acad. Sci. USA **103**, 12323 (2006).
[22] W. Irvine, V. Vitelli, and P. Chaikin, Nature (London) **468**, 947 (2010).
[23] A. Bausch, M. Bowick, A. Cacciuto, A. Dinsmore, M. Hsu, D. Nelson, M. Nikolaides, A. Travesset, and D. Weitz, Science **299**, 1716 (2003).
[24] K. Zahn and G. Maret, Phys. Rev. Lett. **85**, 3656 (2000).
[25] D. Chokappa and P. Clancy, Mol. Phys. **61**, 597 (1987).
[26] N. de Sousa, J. J. Sáenz, F. Scheffold, A. García-Martín, and L. S. Froufe-Pérez, J. Phys.: Condens. Matter **28**, 135101 (2016).

[27] S. Toxvaerd, Phys. Rev. A **24**, 2735 (1981).
[28] R. Bruinsma, B. I. Halperin, and A. Zippelius, Phys. Rev. B **25**, 579 (1982).
[29] R. G. Winkler and A. G. Cherstvy, in *Polyelectrolyte Complexes in the Dispersed and Solid State I* (Springer, Berlin, 2013), pp. 1–56.
[30] M. Pietilä, S. Laurinavičius, J. Sund, E. Roine, and D. Bamford, J. Virol. **84**, 788 (2010).
[31] A. Överby, R. Pettersson, K. Grünewald, and J. Huiskonen, Proc. Natl. Acad. Sci. USA **105**, 2375 (2008).
[32] P. Hanusse and A. Blanché, J. Chem. Phys. **74**, 6148 (1981).
[33] A. B. Bortz, M. H. Kalos, and J. L. Lebowitz, J. Comput. Phys. **17**, 10 (1975).
[34] E. Martínez, J. Marian, M. H. Kalos, and J. M. Perlado, J. Comput. Phys. **227**, 3804 (2008).